



# Structure and electrical properties of nanostructured zinc oxide films prepared for optoelectronic applications

Elmehdi Elakrmi <sup>‡</sup>, Rafik Ben Chaâbane, Hafedh Ben Ouada

*Laboratoire de Physique et Chimie des Interfaces, Département de Physique,  
Faculté des Sciences de Monastir, 5019 Monastir, Tunisia*

Zinc oxide (ZnO) forms nanostructures with optical and transport properties that render them useful for a variety of industrial applications. In this study, ZnO nanostructures were elaborated in the presence of PEG-400 by thermal decomposition of zinc hydroxide formed after precipitation of zinc acetate from aqueous solution. FTIR transmission spectra, scanning electron microscopy (SEM), UV-Visible spectrophotometry, and X-ray diffractometry (XRD) were used to characterize ZnO nanostructures. Inorganic diodes consisting of ZnO layers between indium-tin oxide (ITO) and Al contacts were elaborated. Current-voltage characteristics and the AC electrical response of the consolidated nanoparticles of ZnO were studied using impedance spectroscopy. The equivalent circuit parameters were determined by computer simulation. The grain, grain boundary and electrode interface contributions to the conductivity are discussed.

**KEYWORDS:** ZnO, PEG-400, nanostructures, electrical properties, impedance spectroscopy

**COPYRIGHT:** © 2012 Elakrmi *et al.* This is an open-access article distributed under the terms of the Creative Commons Attribution License, which permits unrestricted use, distribution, and reproduction in any medium, provided the original author and source are credited.

Nanostructure semiconductor metal oxides have drawn much attention during the last few years due to their optical and transport properties, and consequent potential for many optoelectronic applications [1]. Among them, zinc oxide (ZnO) forms versatile materials used in different fields for applications such as solar cells, optical waveguides and gas sensors [2]. These materials have interesting properties such as the high chemical stability and non-toxicity, as well as various morphologies (nanowire, [3] nanobelt, [4] nanoplate, [5] nanotube, [6]), rendering them suitable for nanodevice design.

ZnO is a II-VI-semiconductor with a large band gap of approximately 3.34 eV [7]. It crystallizes in a hexagonal wurtzite structure [8]. Its crystal growth is

strongly influenced by external conditions such as reaction temperature, pH of the solution and the nature of additives [9-10]. The properties of ZnO structure consequently depend strongly on the synthesis method and conditions.

In this paper, we report a simple approach to fabricate ZnO crystalline nanostructure obtained from  $\text{Zn}(\text{OH})_4^{2-}$  in aqueous solution in the presence of short-chain polymer, polyethylene glycol (PEG-400). PEG-400 is a surfactant easily adsorbed at the surface of the metal oxide which modifies the growth kinetics of growing colloids leading ultimately to anisotropic crystallization.

Impedance spectroscopic analysis of ZnO grain and grain boundary properties is accomplished here on Al/ZnO/ITO diode [11] as well as the investigation of their electrical properties via I-V characteristics. Our aim is to give deeper insight into charge-carrier injection and transport mechanisms in the device. The obtained characteristics are simulated to give an electrical

<sup>‡</sup>Correspondence: mehdi.fsm@gmail.com

Received: 24 March 2011; Accepted: 6 July 2011

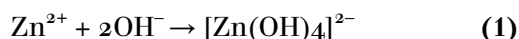
equivalent circuit in order to extract the relaxation times for grain and grain boundary.

## Materials and Methods

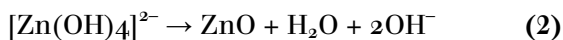
### Nanostructure synthesis

The synthesis of nanostructure zinc oxide was carried out using high purity (> 97%) zinc acetate  $[\text{Zn}(\text{CH}_3\text{COO})_2]$  and sodium hydroxide precursors. Stock solutions were made by dissolving 0.1 M  $\text{Zn}^{2+}$  and 5 M NaOH in 20 mLs distilled water for 60 minutes. Acetic acid was added in order to lower the solution pH, which was ultimately adjusted to 9.5 by adding NaOH at 100  $\mu\text{l}/\text{min}$  while monitoring with an expandable ion analyzer (HI 8519N). The mixture of  $\text{Zn}(\text{Ac})_2$  and NaOH was then stirred in the presence of 1g PEG-400 for 30 min, while the ITO substrate was cleaned in acetone for 15 min. The ZnO films were grown on ITO substrate by the drop-cast method and annealed at 300°C for 3h.

When equivalent volume of zinc acetate dehydrate and NaOH were blended, the reaction precursors,  $[\text{Zn}(\text{OH})_4]^{2-}$  were formed from  $\text{Zn}^{2+}$  and  $\text{OH}^-$  ions:



Subsequent addition of PEG-400 into the reaction mixture modified the growth kinetics of the growing structure, inducing  $[\text{Zn}(\text{OH})_4]^{2-}$  to become needle-shaped. The reaction precursor  $[\text{Zn}(\text{OH})_4]^{2-}$  decomposed to form ZnO nuclei (eq. 2) growing along the direction of the PEG-400 (fig.2).



As the reaction progresses, the function of PEG-400 lessens and agglomerates of needle-shaped ZnO are formed from  $[\text{Zn}(\text{OH})_4]^{2-}$  under hydrothermal conditions [12].

### Sample analysis

The purity of the product was analyzed by the IR spectroscopy and the crystal structure of ZnO the nanoparticles was characterized by X-ray diffractometer equipped with a monochromated  $\text{Cu K}\alpha$  ( $\lambda = 1.54249 \text{ \AA}$ ) radiation. The nanoparticle X-ray diffraction (XRD) patterns were recorded from 25 to 70° in  $2\theta$ . The impedance spectroscopy (IS) and I(V) studies were done on Al/ZnO/ITO heterostructures. These devices consist of a single inorganic ZnO layer sandwiched between two electrodes on top of a glass substrate. They were fabricated on indium tin oxide (ITO)-coated glass substrates (sheet resistance 20 $\Omega$  per unit surface) used as anodes. The ITO substrates were supplied by Merck Display Technologies (MDT). Before the etching process, the ITO substrates were

successively pre-cleaned for 15 min in acetone in an ultrasonic bath and dried by a nitrogen gas flow.

The ITO thin films were used here due to their good efficiency as a hole injection material into inorganic film. The aluminum top electrode was grown on ZnO film by thermal evaporation through appropriately shadow masks in high vacuum conditions ( $10^{-6}$  Torr).

DC measurements were made with a Keithley 236 source measure unit and AC measurements were performed with an HP 4192A LF impedance analyzer. The general term for excitation potential for AC measurements is given by equation 3:

$$V = V_0 + V_{\text{mod}}\cos(\omega t) \quad (3)$$

where  $V_0$  is the DC bias,  $V_{\text{mod}}$  is the oscillation level and  $\omega/2\pi$  is the frequency. In our case, the measurements were performed in the following conditions  $V_0$ : 0-2V and  $V_{\text{mod}}$  of 50 mV over a frequency range of 5Hz-15MHz using a computer controlled HP4192ALF. All electrical measurements were performed in the dark, at room temperature  $T = (23 \pm 5)^\circ\text{C}$ , and with relative humidity (RH%) set to  $55 \pm 5\%$ .

## Results and Discussion

### FTIR spectroscopy

Figure 1 shows the nanostructure IR spectrum which was acquired in the range of 400–4000  $\text{cm}^{-1}$  for the powders calcined at 300°C. Absorption bands near 3400  $\text{cm}^{-1}$  represent O-H mode of vibration, those at 2980  $\text{cm}^{-1}$  are C-H stretching mode and those at 1400-1600  $\text{cm}^{-1}$  are the C=O stretching mode. The band arising from the absorption of atmospheric  $\text{CO}_2$  on the metallic cations at 2350

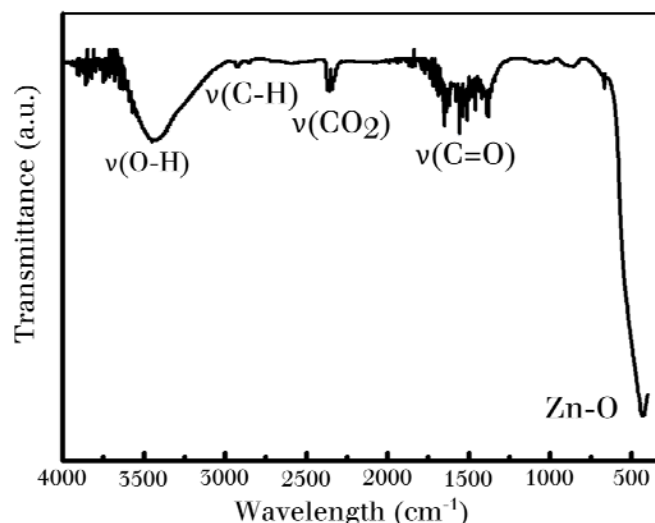


Figure 1. FTIR spectrum of the ZnO nanostructure  $\text{cm}^{-1}$  and bonding between Zn-O ( $434 \text{ cm}^{-1}$ ,  $532 \text{ cm}^{-1}$

<sup>1</sup>) are also visible [13].

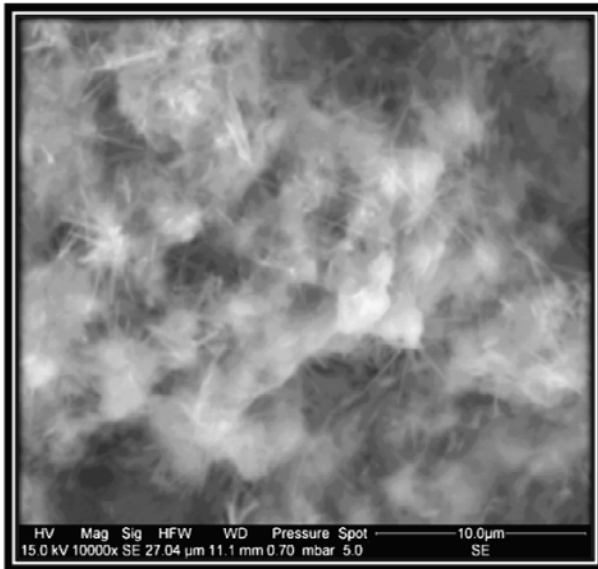


Figure 2. Representative SEM micrograph of the synthesized ZnO nanostructure

#### Scanning electron microscopy

SEM images of ZnO film are presented in **figure 2**. The needle-like morphology of ZnO nanostructures obtained was a result of initial action of PEG-400.

#### X-Ray diffractometry Results

XRD results indicate that the ZnO nanostructure has a crystalline structure with a hexagonal wurtzite structure. The main significant peaks for ZnO nanostructures are (100), (002), (101), (102) and (110), (105), (200), (112) and (201) in seen in **figure 3**.

The crystalline size was evaluated from the XRD data. The width of the Bragg peak is a combination of both instrument-and sample-dependent effects. In order to dissociate these contributions, we collected a diffraction pattern from the line broadening of a standard material, silicon, to determine the instrumental broadening [14]. The corrected instrumental broadening  $\beta_{Si} = 0.075$  rad;  $\beta_{hkl}$  corresponding to the diffraction peak of ZnO was estimated by using **equation 4** [15]:

$$\beta_{hkl} = \left[ (\beta_{hkl})_{measured}^2 - (\beta_{instrument}^2) \right]^{1/2} \quad (4)$$

The crystallite size of the ZnO was determined from  $\beta_{hkl}$  of (1 0 1) diffraction peak using the Scherrer formula:

$$D = \frac{0.89 \lambda}{\beta_{hkl} \cos \theta} \quad (5)$$

Where  $D$ ,  $\lambda$ ,  $\theta$  and  $\beta$  are the mean grain size, the x-ray wavelength and the Bragg diffraction angle of the (101) peak, respectively. The XRD pattern of the sample indicates enhanced intensity for the peak corresponding to (101) plane, indicating preferential orientation along the c-axis. The crystallite size was found to be  $(40 \pm 0.23)$  nm.

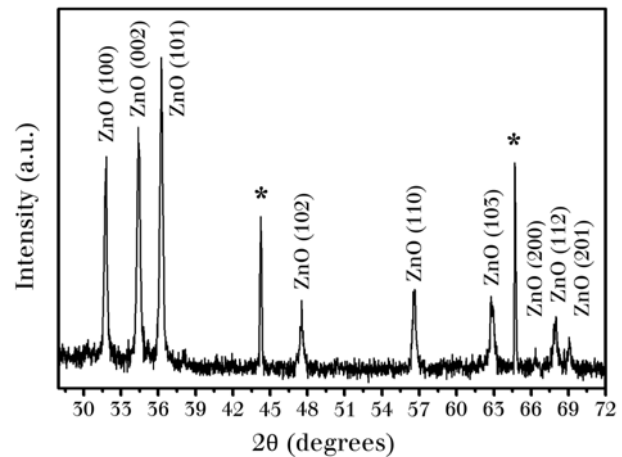


Figure 3. Typical X-ray diffraction pattern of synthesized ZnO nanostructure film deposited on ITO. The labelled peaks correspond to the wurtzite hexagonal phase. (\*) peaks indicate ITO

#### Current-voltage characteristics

**Figure 4** represents the forward and reverse bias current-voltage (I-V) characteristics of the Al/ZnO/ITO structure. In our experiment, we adopted an asymmetric Al/ZnO seed film/ITO contact. The contact between ZnO seed film/ITO junction was a barrier-free ohmic contact due to the lower work function of ITO itself [16]. Therefore, we found that the nonlinear and approximated behavior of the I-V characteristic resulted from the single Schottky contact between the Al and ZnO. The I-V characteristics show typical diode behavior with a threshold bias voltage of 4.98V. The current was observed in both forward and reserve bias voltage. The electrically symmetric I-V characteristic, for low voltages, can be explained by the localized-state theory with defects providing the localized gap states. The asymmetric I-V characteristic at higher voltages is due to the difference of injection barriers to electron and hole due to different work functions for the ITO anode (4.7 eV) and the Al cathode (4.3 eV). The I-V characteristics of the device indicate that this

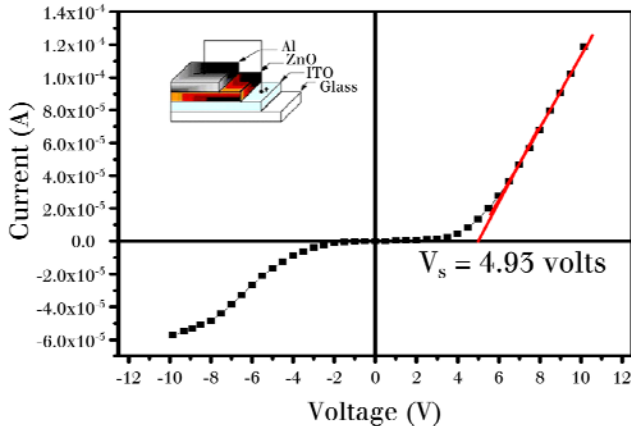


Figure 4. Forward and reverse bias current-voltage characteristics of the Al/ZnO contact on ITO substrate heating in ambient air at room temperature

structure behaves like a Schottky barrier diode in the continuation of an interfacial layer and other effects, the barrier height depends on the bias voltage. Figure 5 shows the forward bias logarithmic plots of the I-V description for the Al/ZnO contact. It is represented by three distinct linear regions, corresponding to changed conduction mechanisms. The existence of these limits is explained by the charge transport profile which influences the slopes of the current-voltage characteristics. At low voltages (I) an ohmic conduction mechanism is dominant where the logarithmic slope is in relation to unity. The ohmic regime with a current density is described by equation 6:

$$J = \frac{e\mu\eta V}{L} \quad (6)$$

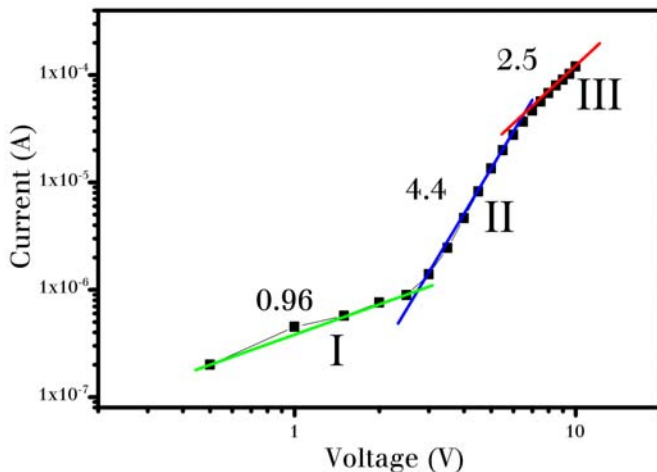


Figure 5. Log-log plot of dark I-V characteristics of the Al-ZnO Schottky diodes measured at room temperature

Where  $V$  is the applied voltage,  $L$  is the thickness of the film,  $\mu$  is the field-independent mobility,  $e$  is the elementary charge and  $\eta$  is the free charge carrier densities.

In this region, injection of charge transporters from the electrodes into the semiconductor material is significantly reduced due to the low bias voltage. At higher voltage level (II) the slope is measured as 4.4, indicating that a space charge-limited current (SCLC) mechanism is controlled by the presence of traps within the band gap of the ZnO. The SCLC regime occurs when the equilibrium charge concentration less than to the injected charge concentration. This drive forms a space charge region near the injecting electrode [17].

When SCLC is dominant, one expects linearity on a plot of  $\log(I)$  versus  $\log(V)$  with a slope of 2 [18]. The high-voltage region corresponds to the trap-free space-charge-limited-current regime, obeying the Mott-Gurney law:

$$J = \frac{9 \epsilon \epsilon_0 \mu \theta V^2}{8 L^3} \quad (7)$$

Where  $V$  is the applied voltage,  $L$  is the thickness of the film, and  $\mu$  is the field-independent mobility. The third region of figure 5 shows a slope of 2. Thus this region also indicates a SCLC mechanism. In this region, the slope of the plot tends to decrease as the device approaches the ‘trap-filled’ limit [19].

#### AC spectroscopy measurements

Impedance spectroscopy was used to study the interface of Al/ZnO/ITO assembly. The variation of conductance and capacitance of ZnO derivative-based diodes versus frequency at different bias voltages were plotted in figures 6 and 7, respectively. Figure 6 shows the frequency dependence on AC conductivity of typical ZnO at different fixed voltages on a log-log scale. At low frequencies AC conductivity was found to be weakly frequency dependent. At all bias voltages the conductivity increases with increasing frequency, though there were different slopes over two frequency regions:

- (I) 0.01–100 kHz; (II) 100–10000 Hz.

Figure 7 illustrates the capacitance measurements as a function of frequency for 0 to 2 V. In general, the interface states in equilibrium with the semiconductor do not contribute to the capacitance at sufficiently high frequencies since the charge at the interface states cannot follow the AC signal. In

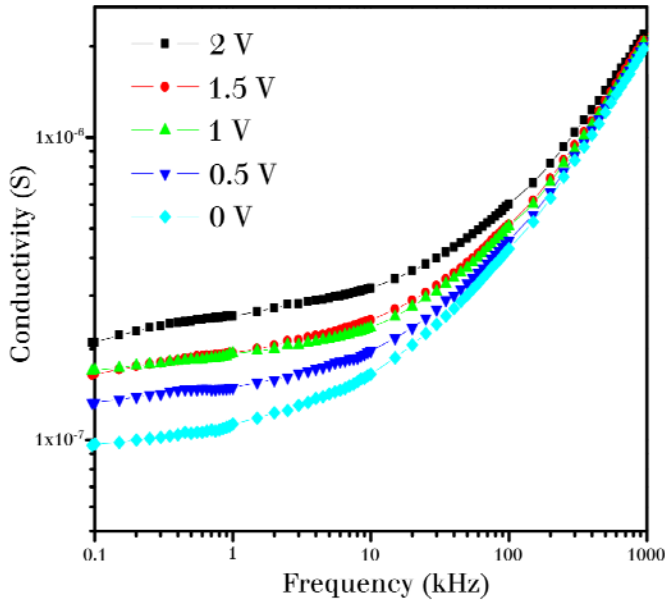


Figure 6. The forward bias conductivity-frequency characteristics of the Al/ZnO contact in different bias voltages heating in ambient air

this case, the capacitance of the diode is the single space charge capacitance [20]. As can be seen in **figure 7**, the capacitance is weakly dependent on frequency, especially at low frequencies. When the frequency was increased further, the capacitance shows strong frequency dependence and tends to decrease. Generally, the capacitance measured for a Schottky diode is dependent on the frequency. The higher values of capacitance at low frequency are due to the excess capacitance resulting from the interface states in equilibrium with the n-type ZnO that can follow the AC signal. From **figure 7**, it can be seen that AC conductance increases with frequency at both voltages and the measurement conductance varies with applied voltage and frequency. This dependence can be attributed to both the presence of the Schottky barrier and impurity levels.

#### Cole-Cole representation

The IS technique consists in the measurement of the electrical impedance  $Z$  as a function of the frequency of the input signal over a wide frequency range (**fig.8**). The composed data was then visualized as Nyquist graph or Cole-Cole plot, represented by the imaginary component  $Z''$  of the impedance as a function of  $Z'$  the real component. The Cole-Cole plots of Al/ZnO/ITO device at several DC bias voltages are shown in **figure 9**. The spectrum exhibits one semicircle asymmetrical part and a

linear part. The low frequency was interpreted as a consequence of the electrode-sample interface. The higher frequency arc is due to the grain and grain boundary effects [21]. This general relaxation is attributed to the inherent properties of the ZnO, since the behavior of the ZnO cannot be adequately drawn by means of frequency-independent resistances and capacitances for all the frequency ranges [22]. Restated, the observed relaxation provides evidence for a deep electronic defect within the depletion regions formed at the grain boundaries of the ZnO. It is neither an electrode effect nor a simple Maxwell-Wagner dielectric relaxation, which is suitable for heterogeneous materials with different resistivity and dielectric constants. It has been concluded by some researchers that the common relaxation is associated with the singly ionized oxygen vacancy [23]. The nonlinearity in nanocrystalline semiconducting oxides has been attributed to the potential barriers at the grain boundaries [24]. To investigate the microstructure components that have contributed to the electrical properties, we used impedance spectroscopy under bias voltages at  $(23 \pm 3^\circ)$  in ambient air. Results are plotted in **figure 9**. Only one semicircle is observed in all applied DC cases. As the bias voltage increases, the diameter of the semicircle becomes smaller. The appearance of a single semicircular response indicates that one component or several components with identical time constants are dominating the electrical properties. The mechanisms which contribute to the electrical properties belong either to a single grain or to an interface such as a grain boundary.

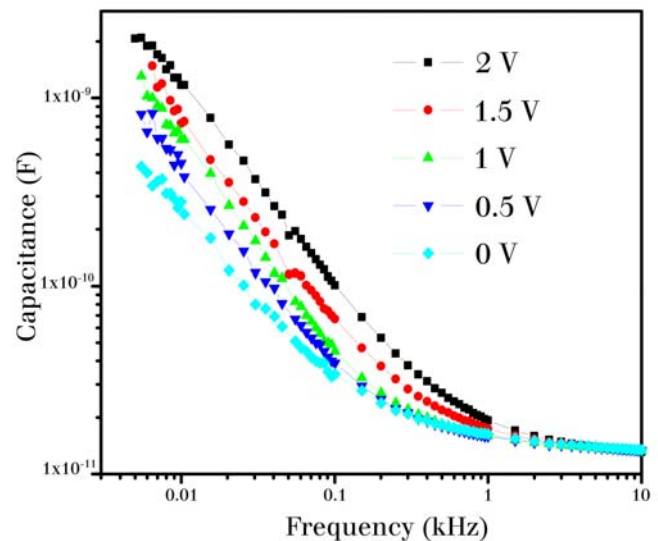


Figure 7. The forward bias capacitance-frequency characteristics of the Al/ZnO contact in different bias voltages heating in ambient air

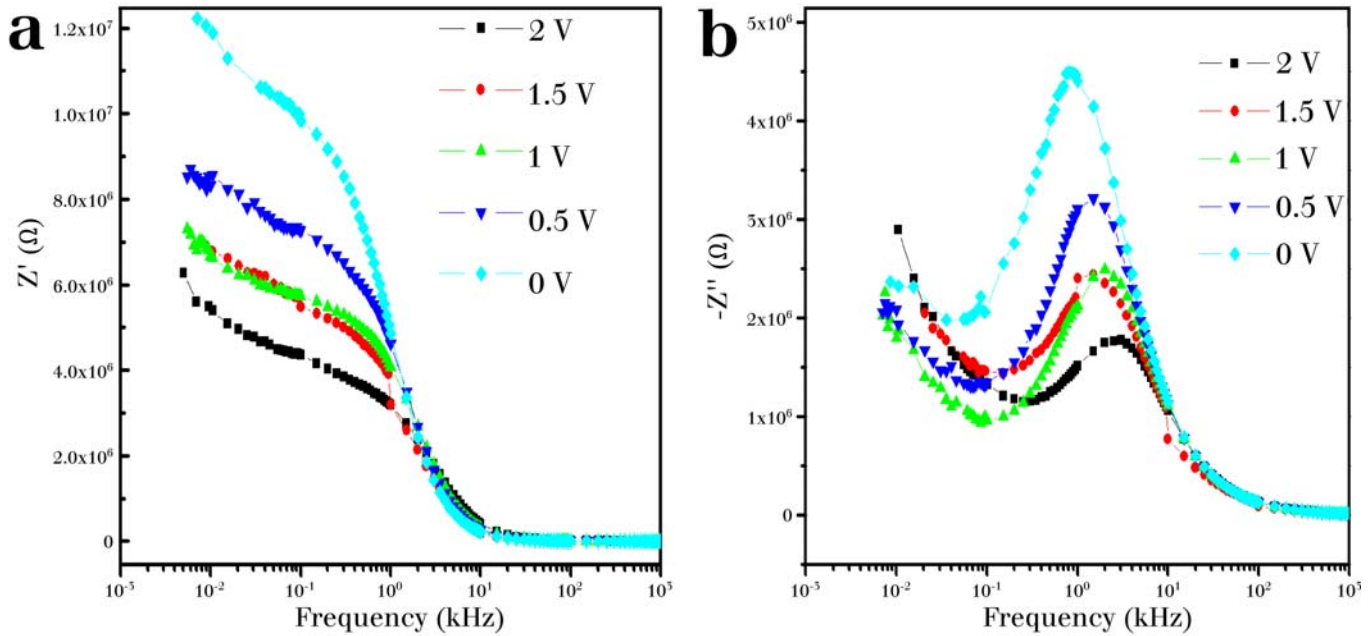


Figure 8. The frequency-dependent real (a) and imaginary (b) part of the impedance of ITO/ZnO/Al at different bias voltages in ambient air

*AC spectroscopy modelling and measurements*

IS results were interpreted in terms of an equivalent circuit (inset of figure 10). In this figure a Constant-Phase Element (CPE) is introduced because the semicircles in the Nyquist plots are depressed due to surface roughness and heterogeneity of the surface [15]. In this case, the impedance of a CPE is given by:

$$\frac{1}{Z_{CPE}} = Q(j\omega)^n \tag{8}$$

Where  $Z_{CPE}$  is the impedance of CPE,  $Q$  is a proportional factor,  $\omega$  is the angular frequency, and  $n$  is a factor which takes values between 0 and 1. In an impedance spectrum, the grain, grain boundary and interface electrode contributions to the conduction process can be easily separated out using the modified Cole–Cole expression and with the aid of an equivalent circuit model.

The ZnO layer is here modeled by a series association of three parallel RC circuits, attributed to grain (g), grain boundary (gb) and interface electrode (Al) ZnO. In this circuit the parallel ( $R,C$ ) elements corresponding to the grain (g), grain boundary (gb) and electrode (e) are connected in series. The total grain resistance ( $R_g$ ), total grain boundary resistance ( $R_{gb}$ ) and the electrode resistance ( $R_e$ ) can be obtained from the intersections on the real axis of the corresponding semicircular arcs. The total grain resistance ( $R_g$ ), total grain boundary resistance ( $R_{gb}$ ) and the electrode resistance ( $R_e$ ) can be obtained from the intersections on the real axis of the corresponding semicircular arcs. The frequency corresponding to the peak of each arc is given by  $\omega_i = 1/R_i C_i$ . Typically the capacitances are such that  $C_e \geq C_{gb} \geq C_g$  and for this reason the high-mid and low-frequency arcs

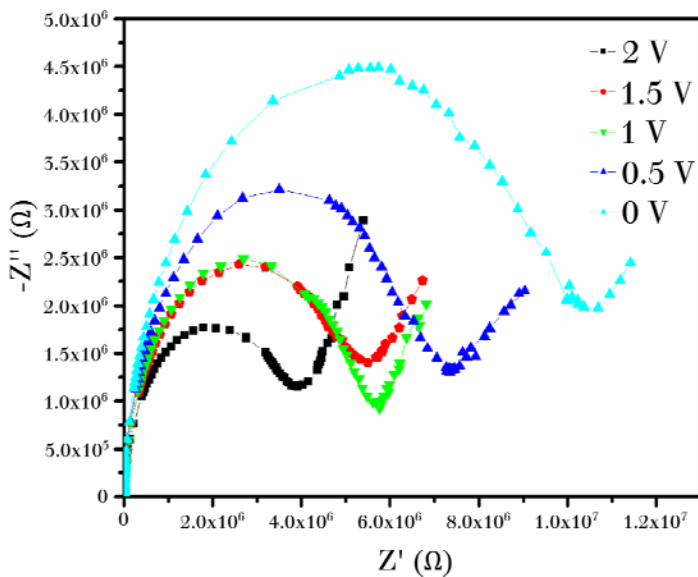


Figure 9. Impedance spectra of Al/ZnO/ITO at various bias voltages heating in ambient air.

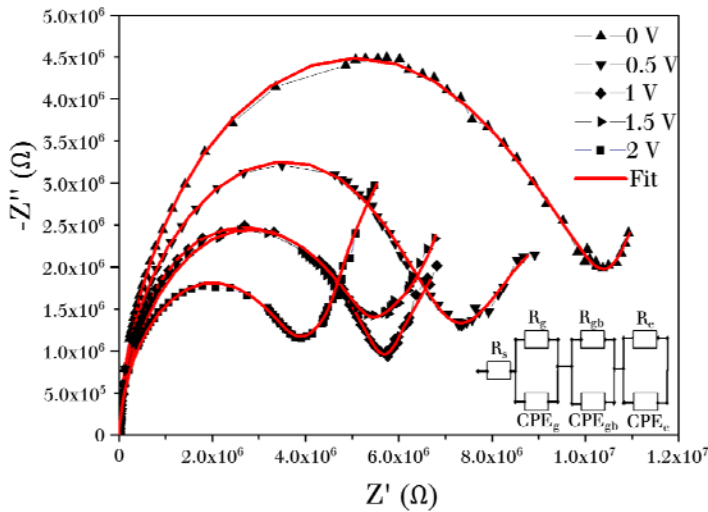


Figure 10. Nyquist plots of the typical device and its fit with an equivalent AC circuit (solid red line) at different bias voltages.

correspond to the grain, grain boundary and electrode–sample interface impedances [20]. Each RC circuit is described by a semicircle and in the complex plane plot of  $Z'$  versus  $Z''$  (Nyquist diagram), the total impedance given by:

$$Z(i\omega) = Z'(\omega) - iZ''(\omega) \tag{9}$$

The deformation of the experimental semicircle arc is taken into description by parameter  $n$ .  $n \approx 1$  corresponds to the parallel combination of pure R and C components, (b)  $n \approx 0$  represents a circuit equivalent to a pure resistance represented by one point in the Nyquist diagram, and the intermediate case  $0 < n < 1$ , represents a scenario in which the diffusion phenomena are described by the parallel combination of a resistance  $R$  and a constant phase element (CPE). The mathematical demonstrations of the  $Z'(\omega)$ , and  $Z''(\omega)$  expressions were performed geometrically [21].

The asymmetric circular diameter in the impedance plane which relates to the resistance of the grain and grain boundaries of the ZnO decreases with rising bias voltages or applied electric field. This, we believe, is due to the increase of conduction charge carriers from the ZnO grains that flow into the grain boundaries. In general, the trapping states within the interface layers are due to various metal oxide additions. There is a large quantity of mobile electrons in the n-type ZnO grains. The electrons tend to diffuse away to reach the interface layers and be trapped by the trapping states, leaving behind a positive fixed charge of ionized donors in the locality of the interface layers. Consequently, a depletion region is formed on both sides of the grain boundary and thus there are a series of Schottky barrier diodes in the ZnO [7-9].

Table 1. Magnitudes of parameters obtained by simulation of experimental data at various bias voltages.

	0V	0.5V	1V	1.5V	2V
$R_s$ (Ω)	21.59	23.46	21.65	23.35	21.52
$R_g$ (Ω)	$1.624043 \times 10^6$	$1.474400 \times 10^6$	$1.393320 \times 10^6$	$1.365620 \times 10^6$	$1.158044 \times 10^6$
$R_{gb}$ (Ω)	$9.014034 \times 10^6$	$8.166465 \times 10^6$	$6.672232 \times 10^6$	$5.968083 \times 10^6$	$4.332980 \times 10^6$
$R_e$ (Ω)	$6.189652 \times 10^6$	$5.026560 \times 10^6$	$4.968082 \times 10^6$	$4.679784 \times 10^6$	$3.121236 \times 10^6$
$C_g$ (F)	$4.541 \times 10^{-6}$	$3.85 \times 10^{-6}$	$3.47 \times 10^{-6}$	$2.71 \times 10^{-6}$	$1.21 \times 10^{-6}$
$C_{gb}$ (F)	$5.97 \times 10^{-7}$	$4.89 \times 10^{-7}$	$3.75 \times 10^{-7}$	$3.7 \times 10^{-7}$	$1.006 \times 10^{-7}$
$C_e$ (F)	$9.72 \times 10^{-6}$	$8.01 \times 10^{-6}$	$7.64 \times 10^{-6}$	$6.09 \times 10^{-6}$	$4.79 \times 10^{-6}$
$n_g$	0.87	0.91	0.89	0.86	0.81
$n_{gb}$	0.93	0.96	0.94	0.94	0.99
$n_e$	0.71	0.71	0.71	0.71	0.71
$\tau_g$ (s)	7.37	5.67	4.83	3.70	1.40
$\tau_{gb}$ (s)	5.38	3.99	2.50	2.20	0.43
$R^2$ (fit)	0.99995	0.99998	0.99992	0.9998	0.9997

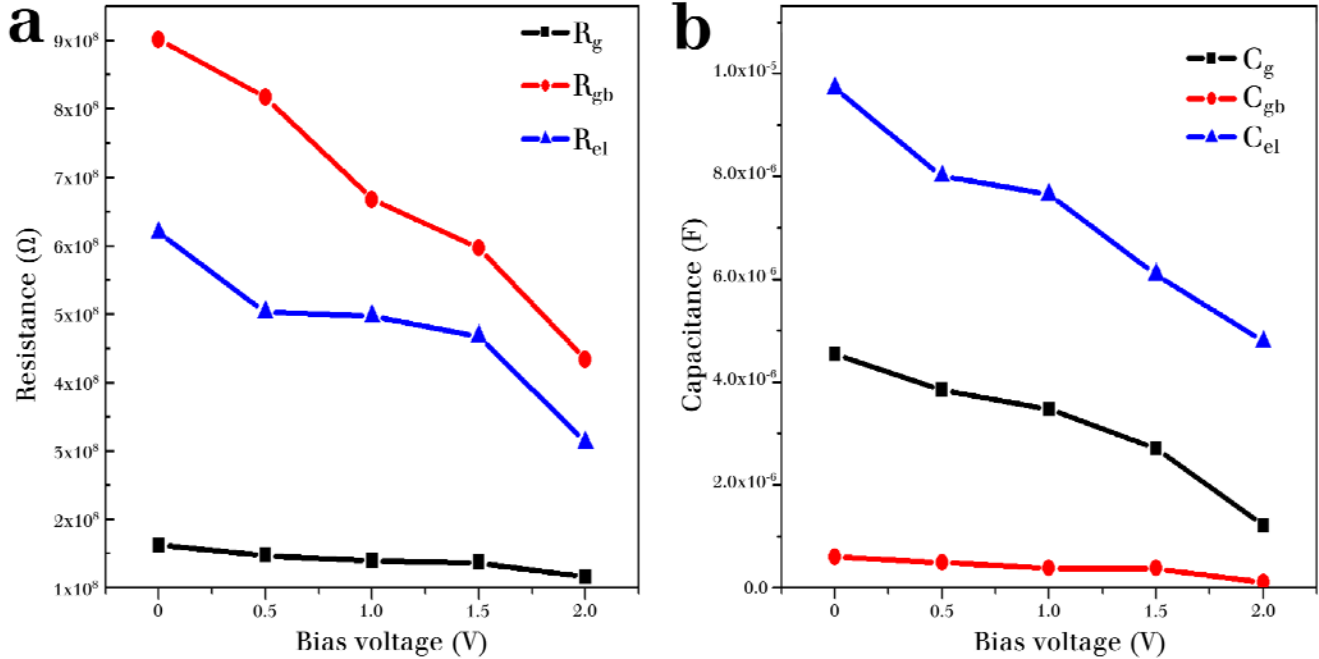


Figure 11. Variations of the fitting parameters for  $R_g$ ,  $R_{gb}$  (a) and  $C_g$ ,  $C_{gb}$  (b) as a function of the DC bias voltage

Therefore, the nature of the interface layer is of considerable interest, the knowledge of which plays an important role in understanding the highly non-ohmic property of the ZnO nanostructure.

The aluminum electrode behavior of our specimens is described in terms of the resistance  $R_e$ , and the capacitance  $C_e$ , in parallel. Our present hypothesis is that  $C_e$  represents the double layer capacity of the electrode, and  $R_e$  represents an effective resistance for the overall electrode reaction [22]. In our case, the redox couple being able to exist has vapor humidity, the rest potential of the Al electrode is mixed potential fixed by the electrochemical reaction:



Impedance spectra of the Al/ZnO/ITO diode at different bias voltages are shown in **figure 10**. These dependences are well-approximated by the CPE equivalent circuit and corresponding parameters are summarized in **table 1**. While the grain boundary resistance decreases with DC bias, grain resistance increases. Our experimental studies showed that the electrical properties of the ZnO are affected by a large number of factors. It was therefore clear that the development of equivalent circuits would be very useful or would be necessary to achieve a better understanding of the characteristics of the ZnO. The time constant  $\tau_{gb}$  decreases as the bias voltages increase (**table 1**), due to the diffusion potential

Schottky barriers, which is in the neighbourhood of the grain boundaries, tends to decrease with rising bias voltages. This occurs as a result of the shift of the Fermi level towards the middle of the forbidden gap [23].

For clarity, the R and C fitting parameters are plotted as a function of DC bias in **figures 11a and 11b** respectively. The observation that  $R_g$  and  $R_{gb}$  decrease with increasing DC bias is reasonable because the oxide grain boundary and metal-oxide interfaces generally contain some defects, which in turn result in the trap of carriers. The trap states can provide conducting channels when carriers are injected from an electrode. The decrease of  $R_g$  and  $R_{gb}$  with increasing  $V_{DC}$  can be related to the increase of conducting channels because of the provision of more injected carriers. Conversely,  $C_g$  and  $C_{gb}$  remain almost unchanged with the increase of DC bias, while  $C_{el}$  decreases with increasing DC bias from 0 to 2V. The independence of  $C_g$  and  $C_{gb}$  on DC bias suggests that the oxide grain and grain boundary act as simple capacitors in spite of the increase of injected carriers by additional DC bias. In contrast, the decrease of  $C_{el}$  with dc bias increase implies the existence of depletion-region-like Schottky barriers in metal-oxide interfaces, likely due to the interfacial polarization effect [24].

## Conclusion

In summary, a needle-like ZnO nanostructure film was effectively obtained by a colloidal solution

method using PEG-400. This method exemplifies the utility of polymer chains to direct the growth of 1D nanomaterials. PEG-400 played an important role in both construction of the nuclei and directing hexagonal wurtzite-type morphology of the ZnO crystal. Current-voltage and electric impedance measurement were used to investigate the transport characteristics of holes Al/ZnO/ITO diodes structures. The fabrication and testing of a ZnO diode have been reported and discussed. The mechanism exhibited symmetric I-V characteristics in both forward and reverse bias.

## Acknowledgements

We would like to acknowledge the support of the Department of Physics at the Faculty of Sciences of Monastir. We would also like to thank Nawfel Sakley for the research facilities used in this work.

## References

1. F. Yakuphanoglu. Electrical characterization and device characterization of ZnO microring shaped films by sol-gel method. *J. Alloys Compd* 507 (2010): 1-23.
2. A. O. Dikovska , P. A. Atanasov , S. Tonchev , J. Ferreira and L. Escoubas. Periodically structured ZnO thin films for optical gas sensor application. *J. Sensors and Actuators A* 140 (2007): 19-23.
3. Y. F. M. Zhang, M. Guo and X. Wang. Studies on the PEG-assisted hydrothermal synthesis and growth mechanism of ZnO microrod and mesoporous microsphere arrays on the substrate. *J. Phys.Lett.* 10 (2010): 1500-1507.
4. Z. W. Pan, Z. R. Dai, and Z. L. Wang, Nanobelts of semiconducting oxides. *J. Science* 291(2001): 1947-1949.
5. F. Xu , Z-Y. Yuan, G-H. Du, M. Halasa and B.L. Su. High-yield synthesis of single-crystalline ZnO hexagonal nanoplates and accounts of their optical and photocatalytic properties. *J. Applied Physics A* 86 (2007):181-185.
6. R.M. Wang , Y.J. Xing, J. Xu and D. P. Yu. Fabrication and microstructure analysis on zinc oxide nanotubes. *New Journal of Physics* 5 (2003): 115.1-115.7.
7. R. N. Bhargava, D. Haranath and A. Mehta. Bandgap Engineering and Doping of ZnO and ZnOS Nanocrystals. *J. Physical Society* 55 (2008): 2847-2851.
8. Y. Chen, R. Yua, Q. Shi, J. Qin and F. Zheng. Hydrothermal synthesis of hexagonal ZnO clusters. *J. MaterialsLetters* 61 (2007): 4438-4441.
9. J. Zhang, L. Sun, J. Yin, H. Su, C. Liao, and C. Yan. Control of ZnO Morphology via a Simple Solution Route. *J. Chem. Mater.* 14 (2002): 4172-4177.
10. R. Wahab, S.G. Ansari , Y. S. Kim, M. Song and H.-S. Shin. The role of pH variation on the growth of zinc oxide nanostructures. *J. Applied Surface Science* 255 (2009): 4891-4896.
11. S-H. Park, S-H. Kim and S-W. Han . Growth of homoepitaxial ZnO film on ZnO nanorods and light emitting diode applications. *J. Nanotechnology* 18 (2007): 2541- 2544.
12. X. Hou, F. Zhou, B. Yu and W. Liu. PEG-mediated synthesis of ZnO nanostructures at room temperature *J. Materials letters.* 61 (2007): 2551- 2555.
13. Erjun Tang, Guoxiang Cheng, Xiaolu, Xingshou Ma, Pang and Qiang Zhao. Surface modification of zinc oxide nanoparticle by PMAA and its dispersion in aqueous system. *J. Applied Surface Science* 252 (2006): 5227-5232.
14. A. Khorsand Zak and W.H. Abd. Majid. Characterization and X-ray peak broadening analysis in PZT nanoparticles prepared by modified sol-gel method. *J. Ceramics International* 36 (2010): 1905-1910.
15. R. Yogamalara, R. Srinivasan , A. Vinu , K. Ariga, A. C. Bose. *J. Solid State Communications* 149 (2009): 1919-1923.
16. C. Ke , G. Cheng, S. Wang, L. Li, S. Dai, X. Zhang, B. Zou and Z. Du. Surface states dominative Au Schottky contact on vertical aligned ZnO nanorod arrays synthesized by low-temperature growth. *J. Phys.* 9 (2007): 214.
17. M. Zhu, T. Cui, K. Varahramyan. Microelectron Experimental and theoretical investigation of MEH-PPV based Schottky diodes. *J. Microelectronic Engineering.* 75 (2004): 269-274.
18. Ş. Aydoğan, K. Çınar, H. Asıl, C. Coşkun and A Türüt. Electrical characterization of Au/n-ZnO Schottky contacts on n-Si. *J. Alloys and Compounds.* 476 (2009): 913-918.
19. S. N. Das, J.H. Choi, J.P. Kar, K.J. Moon, T.I. Lee and J.-M. Myoung. Junction properties of Au/ZnO single nanowire Schottky diode. *J. applied physics letters* 96 (2010): 092111.
20. Ş. Karatas and A Türüt. The determination of interface state energy distribution of the H-terminated ZnO/p-type Si Schottky diodes with high series resistance by the admittance spectroscopy. *J Vacuum* 74 (2004): 45-53.
21. J. R. Macdonald, John Wiley & Sons, New York : Impedance Spectroscopy, Emphasizing Solid Materials and Systems (1987).
22. D.M. Brewis, J. Comyn and A.K Raval . The effect of humidity on the durability of aluminium-epoxide joints. *J. Adhesion and Adhesives* 10 (1990): 247-253.
23. S.-N. Bai and T. Uyen. The effect of grain boundaries in the electrical properties of ZnO based varistor. *J. Electronic Materials*, 21 (1992):111.
24. J. C. A. Huang. Inspection of magnetic semiconductor and clustering structure in CoFe-doped ZnO films by bias-dependent impedance spectroscopy. *J. Applied physics letters.* 87 (2005): 132503.